ACS Photonics

pubs.acs.org/journal/apchd5

Letter

Variable Repetition Rate THz Source for Ultrafast Scanning Tunneling Microscopy

Mohamad Abdo, Shaoxiang Sheng, Steffen Rolf-Pissarczyk, Lukas Arnhold, Jacob A. J. Burgess, Masahiko Isobe, Luigi Malavolti, and Sebastian Loth*

Cite This: *ACS Photonics* 2021, 8, 702−708

Read Online

ACCESS | Metrics & More | Article Recommendations

ABSTRACT: Broadband THz pulses enable ultrafast electronic transport experiments on the nanoscale by coupling THz electric fields into the devices with antennas, asperities, or scanning probe tips. Here, we design a versatile THz source optimized for driving the highly resistive tunnel junction of a scanning tunneling microscope. The source uses optical rectification in lithium niobate to generate arbitrary THz pulse trains with freely adjustable repetition rates between 0.5 and 41 MHz. These induce subpicosecond voltage transients in the tunnel junction with peak amplitudes between 0.1 and 12 V, achieving a conversion efficiency of 0.4 V/(kV/cm) from far-field THz peak electric field strength to peak junction voltage in the STM. Tunnel currents in the quantum limit of less than one electron per THz pulse are readily detected at multi-MHz repetition rates. The ability to tune between high pulse energy and high signal fidelity makes this THz source design effective for exploration of ultrafast and atomic-scale electron dynamics.

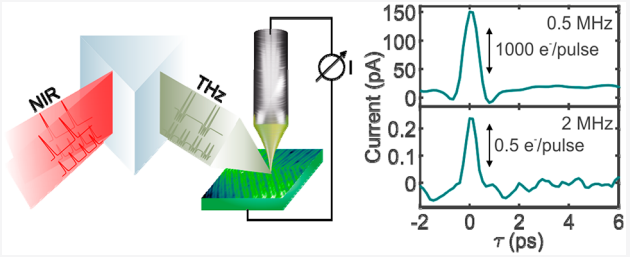

KEYWORDS: *THz generation, variable repetition rate, scanning tunneling microscopy, near-field tip enhancement, THz-coupled STM, pump−probe spectroscopy*

THz light sources lend themselves to spectroscopy of low-energy collective excitations in electronic phases of matter,[1−3] such as superconductivity,[4] charge- and spin-density wave order,[5−7] and electronic insulators.[8] The rapid development of efficient THz generation techniques,[9,10] as well as THz optics,[11] enabled many new spectroscopy and imaging methods.[12−15] They also enable ultrafast electronic transport experiments[16−19] by using lithographically defined antennas[20] or capacitively coupled Auston switches[21] to induce subpicosecond voltage transients in transport devices.[22]

Electric current, directly driven by THz light, scales with the sample resistance and can become vanishingly small for nanoscale devices that consist of nanowires, point contacts, or thin strips of 2D materials. The extreme limit of ultrafast nanoscale transport experiment is the tunnel junction of a scanning tunneling microscope (STM) excited with THz pulses.[15] In this limit, the THz-induced current can be as small as one electron per THz pulse. This enables pump−probe spectroscopy of surfaces and molecules with subpicosecond temporal and atomic-scale spatial resolution.[23,24] However, it poses a significant experimental challenge: in order to create a measurable electric current, the experiment's repetition rate must be maximized, while the THz pulse energy must be sufficiently large to excite the tunnel junction. Thus far, intense THz sources operating at fixed repetition rates of 1 MHz[25,26] or below[23,24] were used. They offer strong THz excitation, but the low repetition rate limits the signal strength of the THz-induced tunnel current.

Here we discuss a versatile THz source in which pulse energy and repetition rate are highly tunable. The source is based on a commercial fiber-amplified femtosecond laser and THz generation in a lithium niobate prism. It delivers single-cycle THz pulses at a center frequency of 0.5 THz with a maximum repetition rate of 41 MHz. The achievable pulse energy ranges between 2.5 pJ at 41 MHz and 8.8 nJ at 0.5 MHz that yield peak electric fields between 400 V/cm and 16 kV/cm with a focused THz beam.

We validate the performance of our THz source by focusing the THz pulses onto the tunnel junction of a variable-temperature STM and measuring the THz-induced tunneling current. Using the electric field waveform of the THz pulse and the $I(V)$ characteristic of the tunnel junction, we determine the peak transient voltage induced by individual THz pulses in the

Received: October 26, 2020
Published: March 8, 2021

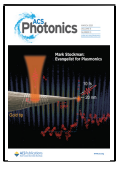

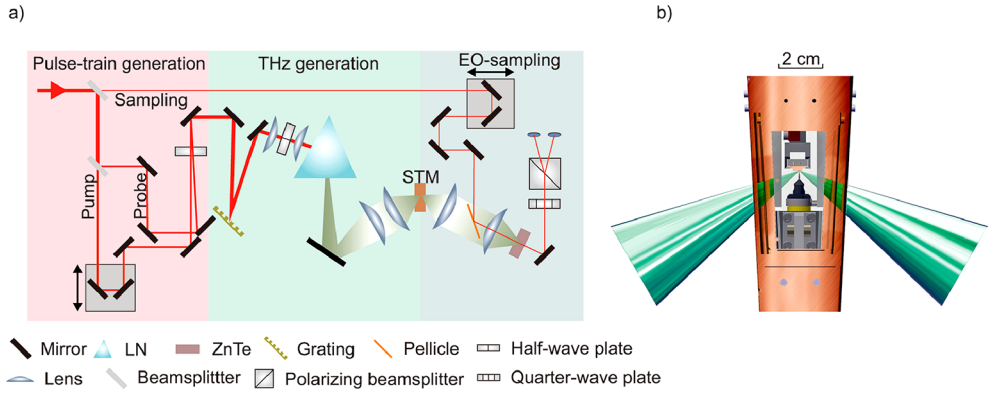

Figure 1. (a) Schematic of the variable repetition rate THz source. Near-infrared beam paths (pump, probe, and sampling) are depicted in red and THz beam paths are depicted in green. Pulses from a fiber-amplified fs-laser enter (red arrow) with 20 W of power and are split into pump (10 W) and probe (10 W) paths and a sampling beam for electro-optic sampling (10 mW). Pulse fronts are tilted by 64° by a grating and imaged into a lithium niobite prism (LN) where they generate THz pulses. These pulses are focused onto the probe tip of a scanning tunneling microscope (STM). THz light scattered from the STM tip is picked up by the electro-optic sampling stage. (b) Sketch of the STM (gray) with cryogenic shields (orange) and two optical access ports with numerical aperture NA = 0.23 (green).

STM junction to range between 120 mV at 41 MHz and 12 V at 0.5 MHz. Thus, tunneling currents ranging from few tens of femtoamperes to hundreds of picoamperes are consistently generated. This enables highly sensitive pump−probe spectroscopy at the limit of less than one electron tunneling per THz pulse. We confirm the applicability by femtosecond pump probe spectroscopy on the metallic Au(111) surface and on Ta_2NiSe_5, an excitonic insulator candidate,[27] where electron dynamics with a time constant of 0.9 ps are resolved.

VARIABLE REPETITION RATE THZ SOURCE

Optical rectification in a stoichiometric $LiNbO_3$ (LN) prism is used to convert arbitrary near-infrared (NIR) fs-laser pulse trains into matching THz pulse trains. Pulse amplitudes and pulse patterns, for example, for pump−probe spectroscopy, are set in the near-infrared beam for which high-efficiency optical elements are readily available and easily adjustable, Figure 1. The THz path to the STM is kept as short as possible with just two polymethyl pentene (TPX) lenses: one to collect the THz light generated in the LN crystal; the other to focus it onto the probe tip of the STM, Figure 1b. Tilted pulse front pumping analogous to ref 28 achieves a high conversion efficiency. A key advantage of this design is that it keeps power losses to a minimum and functions at any repetition rate and over a wide range of pulse energies.

The NIR laser source is a commercial ytterbium-doped fiber laser system (Amplitude Systems Satsuma HP2) that delivers a constant output power of 20 W for repetition rates between 0.5 and 41 MHz. The near-infrared laser pulses have a central wavelength of 1032 nm and a duration of 250 fs. After pulse front tilting with a blazed grating (1500 l/mm) and imaging into the LN crystal, these NIR pulses generate single-cycle THz pulses with a center frequency of 0.5 THz.

We characterize the achieved THz pulse intensity at different repetition rates, as well as the profile of the THz focus, by placing a commercial power meter and a custom-built calibrated THz thermopile detector at the position of the STM tip. To allow easy conversion from average power to pulse energy, the beam splitter is replaced by a mirror such that the entire laser power is fed through the probe pulse pathway. The TPX lenses that image the THz beam onto the STM tip achieve a focal spot of 1.7 ± 0.1 mm diameter that remains constant for all repetition rates. Figure 2a shows the dependence of the generated THz pulse energy, S_{THz}, on the NIR pulse energy, S_{IR}. At 41 MHz, the 0.5 μJ NIR pulses generate 2.5 pJ THz pulses, corresponding to a conversion efficiency of 5.1×10^{-6}. As we decrease the laser repetition rate, the NIR pulse energy and, consequently, the generated THz pulse energy increase. At 0.5 MHz, the 40 μJ NIR pulses

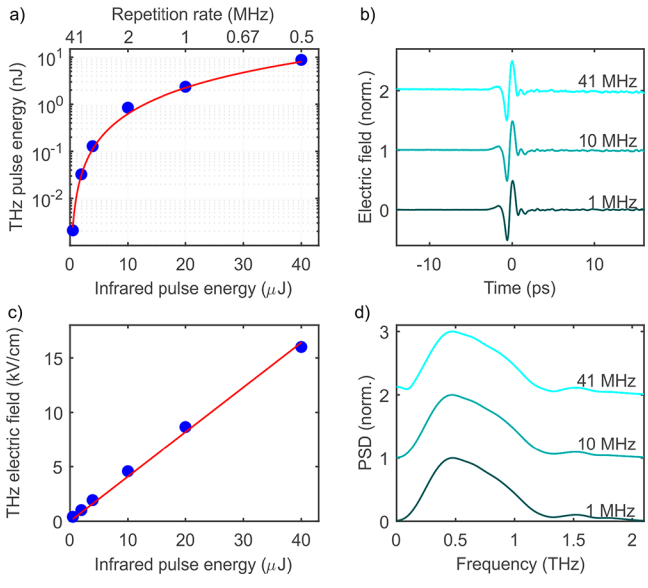

Figure 2. (a) Measured THz pulse energy, S_{THz}, as a function of near-infrared pulse energy, S_{IR} (blue circles), with power law fit: $S_{THz} \propto S_{IR}^{1.8\pm0.2}$ (red curve). S_{IR} is tuned by changing the laser repetition rate from 0.5 to 41 MHz at constant output power. (b) Electric field waveform of the THz pulses at three repetition rates measured by electro-optic sampling. The waveform remains constant for all repetition rates. Pulses are normalized and vertically offset for clarity. (c) Peak electric field of the THz pulses in the focus at the STM tip as a function of NIR pulse energy (blue circles) with linear fit, $E_{THz} = \left(0.41\frac{kV}{cm\cdot\mu J} \pm 0.04\frac{kV}{cm\cdot\mu J}\right)\cdot S_{IR}$ (red curve). (d) Power spectral density, PSD, obtained by fast Fourier transformation of the THz pulses shown in (b). The spectral weight cuts off strongly for frequencies higher than 1.2 THz and shows only minimal variation with repetition rate.

https://dx.doi.org/10.1021/acsphotonics.0c01652
ACS Photonics 2021, 8, 702−708

generate 8.8 nJ THz pulses, corresponding to a conversion efficiency of 2.2×10^{-4}. This fits to the expected behavior of optical rectification and is similar to previous reports of efficient THz generation in LN at room temperature.[29]

A power law fit of the form $S_{THz} = \gamma S_{IR}^{n}$ finds $n = 1.8 \pm 0.2$, that is, the NIR to THz conversion scales approximately quadratically with incident NIR pulse energy.

The electric field waveforms of the THz pulses are measured using electro-optic sampling, Figure 2b. To this end, the THz focus at the position of the STM head is imaged into a ZnTe crystal with a second pair of TPX lenses and sampled with a NIR beam (see Figure 1a). The single-cycle THz pulses have a period of 2 ps, corresponding to a center frequency of 0.5 THz. The residual electric field oscillations following the main pulse ($t > 3$ ps) can mostly be attributed to absorption of THz light in ambient air.[30] Fast Fourier transformation of the electric field waveforms shows that the majority of the spectral weight is distributed between 0.1 and 1.1 THz (Figure 2d). Importantly, the spectra stay nearly identical for all repetition rates. Minor variations at 1 THz and above 1.5 THz may be attributed to small repetition-rate-dependent changes of the NIR pulse shape.

We calculate the peak electric field in the THz focus by normalizing the measured pulse waveform to the measured pulse energy and focus size at the STM tip. At 0.5 MHz repetition rate the THz electric field reaches 16 kV/cm. This reduces to 400 V/cm at 41 MHz, Figure 2c. A linear fit $E_{THz} = \beta \times S_{IR}$ matches well to the measured fields consistent with a linear dependence of THz electric field on incident NIR intensity.

This range of tunability allows for balancing between high THz pulse energies and high repetition rates enabling ultrafast transport experiments with exceptional signal quality. In particular, the achieved pulse energies are sufficient for pump–probe spectroscopy experiments in which the first pulse (pump) excites the device under test and the second (probe) samples its electronic properties at a set delay.

To demonstrate the ultrafast spectroscopy capability of this THz source, we split the NIR beam with a 50:50 beam splitter into two beam paths, a pump and a probe path (Figure 1) and introduce a time delay between them with a linear delay stage in the pump path. The two NIR beams are focused into the LN crystal with a small separation of <0.1 mm between them. This prevents interference between the NIR pulses and, at the same time, guarantees that the generated THz pulses spatially overlap at their focal point in the STM, which is significantly larger than 0.1 mm.

We characterized the electric field waveforms of the pump and probe pulses with different time delays by focusing the THz beam onto the STM tip near its apex and measuring the scattered THz light by electro-optic sampling. The incident optical beam is aligned 60° relative to the tip to minimize shadowing from sample holder and tip. Equivalently, the electro-optic sampling stage is also aligned at 60° relative to the tip. This ensures that the measured THz waveforms are comparable to the electric field waveforms at the position of the STM tip. We placed the STM such that the Gouy phase shifts the carrier-envelope phase by $\pi/2$ with respect to the THz pulse shown in Figure 2b.[31] This makes the THz waveform highly asymmetric and maximizes the peak electric field in the tunnel junction.

Figure 3a shows the resulting electric field waveform for several time delays between pump and probe THz pulses. At

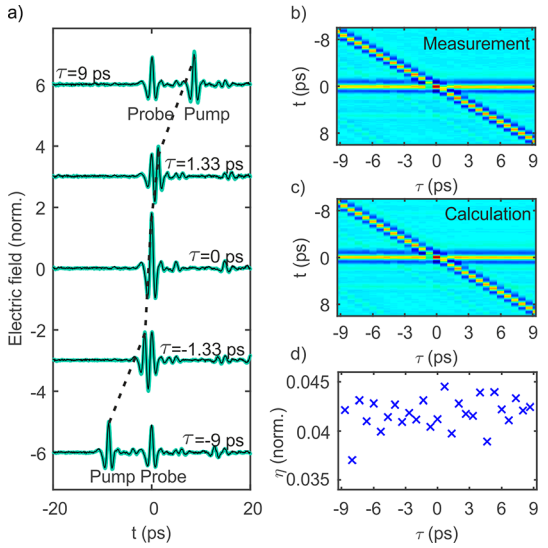

Figure 3. (a) Electric field waveform of the generated THz double pulses for several time delays, τ, between pump and probe pulses, as set by a delay stage in the pump path. Measured data (green curves) are superimposed with calculated time traces of the combined electric field, $E_{THz}(t, \tau)$, (thin black). Waveforms are normalized and offset vertically for clarity. (b, c) Measured and calculated electric field waveforms as a function of t and τ, showing the pump pulse shifting across the probe pulse without affecting it. (d) Normalized root-mean-square deviation, η, between measured and calculated THz double pulses from (b) and (c). The deviation is very small and independent of τ.

large delays ($\tau = \pm 9$ ps), two independent and near-identical phase-stable THz pulses are generated. Indeed, their shapes differ from the pulses shown in Figure 2b, consistent with a $\pi/2$ shift of the Gouy phase. The pump pulse has an approximately 10% larger electric field peak which can be attributed to a small difference in the NIR intensities in the two beam paths. Two small echo peaks are observed 5 and 15 ps after each pulse. These carry less than 1% of the THz pulse energy and are originating from back reflections in the setup.

At short time delays, the electric fields of the pump and probe pulses interfere, creating a combined pulse shape (Figure 3a, $\tau = -1.3$, 0, +1.3 ps). To elucidate whether the two pulses interfere by simply summing their respective THz fields or whether additional modifications occur, we scanned the pump across the probe pulse while repeatedly recording the combined electric field waveforms (Figure 3b). The color-coded plots show that the pump pulse, including its back reflections, moves linearly with delay time. The recorded waveforms can be reproduced well by assuming that the combined waveform, $E_{THz}(t, \tau)$, is simply the sum of the individual pulses, $E_{pump}(t, \tau)$ and $E_{probe}(t)$, where τ is the pump–probe delay (Figure 3c).

$$E_{THz}(t, \tau) = E_{pump}(t, \tau) + E_{probe}(t)$$

Importantly, both pulses conserve their waveform, irrespective of delay time. We find the root-mean-square deviation between measured and modeled waveform to be uniform and independent of τ (Figure 3d). This is consistent with the LN crystal having no time-dependent response to the NIR pulses on the picosecond scale, which would always modify the second pulse, that is, the pump pulse for negative delays and the probe pulse for positive delays. This observation also

https://dx.doi.org/10.1021/acsphotonics.0c01652
ACS Photonics 2021, 8, 702–708

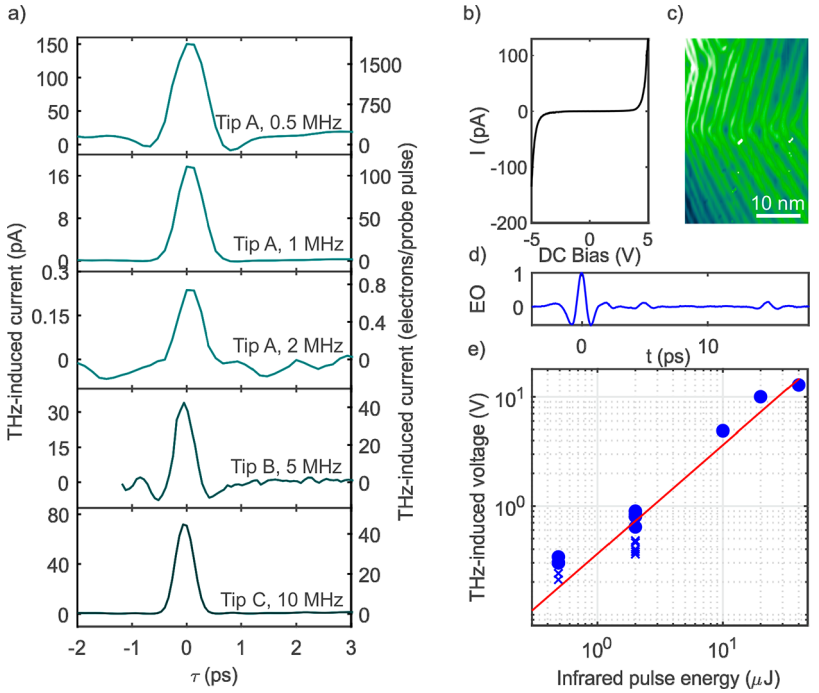

Figure 4. THz-induced tunnel current in the scanning tunneling microscope. (a) Pulse−pulse correlation measurement in the STM for different repetition rates and tips, recording tunnel current while sweeping the delay, τ, between pump and probe pulses. Signal measured on Au(111) with electrochemically etched PtIr probe tips by lock-in detection upon chopping the probe pulse on and off and STM feedback loop closed. Tunnel junction set point for tip A: V_{set} = 100 mV, I_{set} = 100 pA; for tip B: 1 mV, 500 pA; and for tip C: 22 mV, 130 pA. (b) $I(V)$ characteristic of the tunnel junction between the tip and Au(111) surface recorded using a DC bias voltage without THz excitation. The current increases nonlinearly with increasing bias, allowing for rectification of the ultrafast THz electric field. (c) STM image of the Au(111) surface: V_{set} = 100 mV, I_{set} = 100 pA. (d) The electric field waveform of the THz pulse used to calculate the THz-induced voltage for τ = 0 ps. Waveform measured with electro-optic sampling (EO) and normalized to 1 at t = 0 ps. (e) Peak THz-induced voltage in the tunnel junction, $V_{THz}(t = 0, \tau = 0)$, as a function of NIR pulse energy. Data shown for 10 as-etched tips (blue circles) and 8 tips after nanoscale modification of the tip apex (blue crosses) measured on Au(111) and samples with different nonlinearity in their $I(V)$. A linear fit (red) yields the average conversion efficiency $\tilde{\alpha} = 0.18 \frac{V}{\mu J} \pm 0.01 \frac{V}{\mu J}$.

indicates that interference of the NIR pulses in the LN crystal is negligible. Otherwise, the electro-optic sampling traces would show significant variations of the waveform for delays $|\tau| < 0.25$ ps. Both THz pulses are thus generated independently of each other in the LN crystal, and their electric fields sum in the THz focus.

THZ-INDUCED VOLTAGE PULSES IN THE STM

The electric field of the THz pulses couples to the metallic probe tip and, thereby, into the tunnel junction, where it induces a transient bias voltage and tunneling of electrons between tip and sample.[15] We investigate this process using highly conductive metals for the tip (PtIr) and an atomically flat Au(111) surface (Figure 4c) since their electronic response can be considered instantaneous in the picosecond range.[32]

Figure 4a shows pulse−pulse correlation measurements obtained by illuminating the STM tunnel junction with THz light while sweeping the pump pulse across the probe pulse. The THz-induced current peaks at τ = 0 and falls off within 260 fs (80−20% transition) with increasing delay. This modulation on the hundreds of femtosecond scale confirms that the electron tunneling is driven by the electric field of the THz pulse[31] and enables electronic spectroscopy with femtosecond time and atomic-scale spatial resolution.[23,24]

At 0.5 MHz, the THz-induced tunnel current reaches 150 pA at τ = 0 ps and falls off to 21 pA for large delays when the pump and probe pulse do not overlap anymore (Figure 4a, tip A). The maximum current decreases to 17 pA at 1 MHz and further to 240 fA at 2 MHz. Different tips show different current magnitudes, but follow the same trend (Figure 4a, tips B and C). The measured current can be related to the net number of electrons tunneling per single THz pulse by dividing it with the repetition rate and electron charge.

Up to 1900 electrons tunnel per intense THz pulse at 0.5 MHz. Weaker THz pulses induce tunneling of much fewer electrons. Owing to the increased signal quality afforded by the concomitantly higher repetition rates, these miniscule tunneling currents remain detectable. As little as 0.4 electrons per pulse were reliably detected, Figure 4a, demonstrating that this THz source enables experiments in the quantum limit of single electron tunneling.

The nonlinear $I(V)$ characteristic of the tunnel junction acts as a rectifier leading to the net current that can be measured. This current can be expressed as

$$\bar{I}(\tau) = \int \sigma(V_{THz}(t, \tau)) \cdot V_{THz}(t, \tau) dt$$

where $\sigma(V)$ is the conductance of the tunnel junction and V_{THz} is the transient bias voltage, which can be determined by conventional tunneling spectroscopy, Figure 4b. Thus, the net current $\bar{I}$ depends only on the delay time, τ, between the pump and probe pulse, analogous to a field cross-correlation.

In the absence of ps-scale time-dependent processes in the tip or the sample, the transient bias voltage is expected to be proportional to the electric field of the THz waveform[24] (shown for τ = 0 ps in Figure 4d): $V_{THz}(t, \tau) = \alpha E_{THz}$, where α

https://dx.doi.org/10.1021/acsphotonics.0c01652
ACS Photonics 2021, 8, 702−708

is the coupling efficiency to the tunnel junction. Hence, V_{THz} can be extracted quantitatively by fitting $\bar{I}$ to the measured pulse−pulse correlation with α as the only free parameter.

To estimate the conversion efficiency between THz far-field intensity and local tunnel junction voltage that can typically be achieved with PtIr tips, we measured pulse correlations with 18 tips or tip apex configurations on Au(111) and other samples with different nonlinearities in their $I(V)$ characteristics, Figure 4e. We find the THz-induced voltage varies significantly between different tips, indicating that the nanoscopic shape of the tip apex is important for THz coupling to the tunnel junction. Indeed, the coupling efficiency changes by indenting the tip into the Au surface by as little as 1 nm.

Overall, we observe an approximately linear scaling between peak voltage in the tunnel junction and peak electric field strength in the THz focus. The conversion efficiency is $\alpha = 4 \times 10^{-4}$ cm $\pm 2 \times 10^{-5}$ cm, or $\tilde{\alpha} = 0.18 \frac{\mathrm{V}}{\mu\mathrm{J}} \pm 0.01 \frac{\mathrm{V}}{\mu\mathrm{J}}$, if expressed relative to the NIR pulse energy. Note that the standard deviation given here signifies the statistical variation between different STM probe tips; the measurement uncertainty is significantly smaller. Thus, our THz source can induce ultrafast voltage pulses in the STM junction with peak voltages ranging between 100 mV and 12 V.

FEMTOSECOND DYNAMICS IN THE SINGLE-ELECTRON TUNNELING REGIME

We evaluate the capability of this THz source for sensitive measurements of the ultrafast dynamics of correlated electron materials. A recent example is Ta_2NiSe_5, a candidate for an excitonic insulator in which spontaneous condensation of excitons opens a gap in the density of states at the Fermi energy. Since the gap size and with it the nonlinearity of the $I(V)$ curve depend on the exciton density, the THz-induced tunneling current can be expected to change upon excitation. Ultrafast dynamics that manifest in the order parameter were recently reported using far-field optical spectroscopy.[33] STM measurements at 180 K, below the phase transition temperature,[27] show the row-like electronic surface modulation caused by the quasi one-dimensional Ni and Ta chains,[34] Figure 5a, and the highly nonlinear $I(V)$ characteristic close to zero bias in spectra of the differential conductivity, $\mathrm{d}I/\mathrm{d}V$, Figure 5c.

The THz pump probe spectrum, Figure 5b, is markedly different from the pulse−pulse correlation spectra shown in Figure 4a. In addition to the pulse correlation signal, it shows a prominent exponential recovery of the THz-induced current with a characteristic decay constant $\tau_0 = 0.9 \pm 0.1$ ps. The signal is mostly uniform within the surface unit cell with only little variations of the decay constant when the STM tip is above the Ta or Ni chains. A comprehensive understanding of the dynamics is beyond the scope of this report, but it is worth noting that the observed recovery, τ_0, is comparable to the population dynamics of photoinduced carriers in this material.[33]

The THz-induced current remains well below one electron per pulse. The signal peaks at 0.12 electrons per pulse ($\tau = 0$ ps), and the ultrafast recovery has a signal magnitude of only 0.04 electrons per pulse. This highlights the advantage of using a high repetition rate source for ultrafast measurements in the STM: whereas the measurement's noise floor of 35 fA is comparable to previous reports of THz-coupled STM,[35] the high repetition rate of 41 MHz transduces this to a minimum detectable THz-induced current of 5×10^{-3} electrons per pulse and enables measurements in the quantum limit of single-electron tunneling.

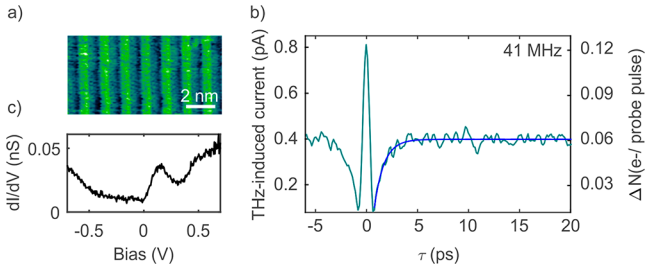

Figure 5. (a) STM image of the Ta_2NiSe_5 surface. Tunnel junction set point V_{set} = 670 mV, I_{set} = 25 pA. (b) Ultrafast response of Ta_2NiSe_5 measured with THz pump−probe spectroscopy (green) by recording the THz-induced tunnel current while sweeping the delay τ. Right axis shows number of electrons tunneling per probe pulse, ΔN. Repetition rate 41 MHz, peak pulse voltage 0.1 V. Feedback loop was open and no offset bias was applied during the measurement. Tunnel junction set point V_{set} = 10 mV, I_{set} = 2 nA. Fitting the dynamic response for $\tau > 0.8$ ps (blue) with an exponential function yields a characteristic decay time of the THz-induced dynamics of $\tau_0 = 0.9 \pm 0.1$ ps. (c) Spectrum of the differential conductivity, $\mathrm{d}I/\mathrm{d}V$, measured on Ta_2NiSe_5 using lock-in detection with 10 mV modulation voltage. V_{set} = 700 mV and I_{set} = 30 pA. All measurements performed at 180 K.

CONCLUSION AND OUTLOOK

We demonstrated an efficient THz source with tunable repetition rate between 0.5 and 41 MHz. THz pulses are generated by optical rectification of 1032 nm pulses inside a lithium niobate prism. A low-loss optical setup delivers the full pump laser power for efficient THz generation. When focused onto the tunneling junction of a scanning tunneling microscope, the generated THz pulses induce ultrafast voltage pulses with peak values of up to 12 V at 0.5 MHz repetition rate. By increasing the repetition rates into the multi-MHz range, the signal fidelity improves and enables measurements of minute THz-induced tunnel currents that reach the quantum limit of less than a single electron tunneling per pulse.

In essence, our THz source enables a smooth transition from experiments with intense THz pulses at low repetition rates to experiments with low intensity pulses at high repetition rates. It becomes possible to balance between high pump power and high-signal-to-noise ratio afforded by higher repetition rates for each experiment. This makes this source design uniquely suited for a broader class of ultrafast transport experiments on the nanoscale, such as spin-torque oscillators, nonequilibrium transport in electro-migration junctions, correlated-electron material research, and high speed electronics based on 2D materials.

AUTHOR INFORMATION

Corresponding Author

Sebastian Loth − *University of Stuttgart, Institute for Functional Matter and Quantum Technologies, 70569 Stuttgart, Germany; Max Planck Institute for Solid State Research, 70569 Stuttgart, Germany; Max Planck Institute for the Structure and Dynamics of Matter, 22761 Hamburg, Germany;* orcid.org/0000-0002-1587-3678; Email: sebastian.loth@fmq.uni-stuttgart.de

https://dx.doi.org/10.1021/acsphotonics.0c01652
ACS Photonics 2021, 8, 702−708

Authors

Mohamad Abdo − *University of Stuttgart, Institute for Functional Matter and Quantum Technologies, 70569 Stuttgart, Germany; Max Planck Institute for Solid State Research, 70569 Stuttgart, Germany; Max Planck Institute for the Structure and Dynamics of Matter, 22761 Hamburg, Germany;* orcid.org/0000-0002-6992-942X

Shaoxiang Sheng − *University of Stuttgart, Institute for Functional Matter and Quantum Technologies, 70569 Stuttgart, Germany*

Steffen Rolf-Pissarczyk − *Max Planck Institute for Solid State Research, 70569 Stuttgart, Germany; Max Planck Institute for the Structure and Dynamics of Matter, 22761 Hamburg, Germany*

Lukas Arnhold − *University of Stuttgart, Institute for Functional Matter and Quantum Technologies, 70569 Stuttgart, Germany*

Jacob A. J. Burgess − *Department of Physics and Astronomy, University of Manitoba, Winnipeg MB R3T 2N2, Canada*

Masahiko Isobe − *Max Planck Institute for Solid State Research, 70569 Stuttgart, Germany*

Luigi Malavolti − *University of Stuttgart, Institute for Functional Matter and Quantum Technologies, 70569 Stuttgart, Germany; Max Planck Institute for Solid State Research, 70569 Stuttgart, Germany*

Complete contact information is available at: https://pubs.acs.org/10.1021/acsphotonics.0c01652

Notes

The authors declare no competing financial interest.

■ ACKNOWLEDGMENTS

The authors thank Björn Schlie for expert technical assistance and A. Cavalleri, A. Cavalieri, I. Grguras and S. Rajasekaran for support. J.A.J.B. and S.S. acknowledge fellowships from the Alexander von Humboldt Foundation, S.R.P. from the German Academic Scholarship Foundation, and J.A.J.B. from the Natural Sciences and Engineering Research Council of Canada. This project has received funding from the European Research Council (ERC) under the European Union's Horizon 2020 Research and Innovation Program (ERC-2014-StG-633818-dasQ).

■ REFERENCES

(1) Baxter, J. B.; Guglietta, G. W. Terahertz Spectroscopy. *Anal. Chem.* **2011**, *83* (12), 4342−4368.

(2) Nicoletti, D.; Cavalleri, A. Nonlinear Light−Matter Interaction at Terahertz Frequencies. *Adv. Opt. Photonics* **2016**, *8* (3), 401−464.

(3) Tanaka, K.; Hirori, H.; Nagai, M. THz Nonlinear Spectroscopy of Solids. *IEEE Trans. Terahertz Sci. Technol.* **2011**, *1* (1), 301−312.

(4) Matsunaga, R.; Hamada, Y. I.; Makise, K.; Uzawa, Y.; Terai, H.; Wang, Z.; Shimano, R. Higgs Amplitude Mode in the BCS Superconductors $Nb_{1-x}Ti_xN$ Induced by Terahertz Pulse Excitation. *Phys. Rev. Lett.* **2013**, *111* (5), 1−5.

(5) Kida, N.; Tonouchi, M. Spectroscopic Evidence for a Charge-Density-Wave Condensate in a Charge-Ordered Manganite: Observation of a Collective Excitation Mode in $Pr_{0.7}Ca_{0.3}MnO_3$ by Using THz Time-Domain Spectroscopy. *Phys. Rev. B: Condens. Matter Mater. Phys.* **2002**, *66* (2), 1−8.

(6) Kampfrath, T.; Sell, A.; Klatt, G.; Pashkin, A.; Mährlein, S.; Dekorsy, T.; Wolf, M.; Fiebig, M.; Leitenstorfer, A.; Huber, R. Coherent Terahertz Control of Antiferromagnetic Spin Waves. *Nat. Photonics* **2011**, *5* (1), 31−34.

(7) Kim, K. W.; Pashkin, A.; Schäfer, H.; Beyer, M.; Porer, M.; Wolf, T.; Bernhard, C.; Demsar, J.; Huber, R.; Leitenstorfer, A. Ultrafast Transient Generation of Spin-Density-Wave Order in the Normal State of $BaFe_2As_2$ Driven by Coherent Lattice Vibrations. *Nat. Mater.* **2012**, *11* (6), 497−501.

(8) Liu, M.; Hwang, H. Y.; Tao, H.; Strikwerda, A. C.; Fan, K.; Keiser, G. R.; Sternbach, A. J.; West, K. G.; Kittiwatanakul, S.; Lu, J.; Wolf, S. A.; Omenetto, F. G.; Zhang, X.; Nelson, K. A.; Averitt, R. D. Terahertz-Field-Induced Insulator-to-Metal Transition in Vanadium Dioxide Metamaterial. *Nature* **2012**, *487* (7407), 345−348.

(9) Blanchard, F.; Sharma, G.; Razzari, L.; Ropagnol, X.; Bandulet, H. C.; Vidal, F.; Morandotti, R.; Kieffer, J. C.; Ozaki, T.; Tiedje, H.; Haugen, H.; Reid, M.; Hegmann, F. Generation of Intense Terahertz Radiation via Optical Methods. *IEEE J. Sel. Top. Quantum Electron.* **2011**, *17* (1), 5−16.

(10) Lewis, R. A. A Review of Terahertz Sources. *J. Phys. D: Appl. Phys.* **2014**, *47* (37), 374001.

(11) Neu, J.; Krolla, B.; Paul, O.; Reinhard, B.; Beigang, R.; Rahm, M. Metamaterial-Based Gradient Index Lens with Strong Focusing in the THz Frequency Range. *Opt. Express* **2010**, *18* (26), 27748−27757.

(12) Guerboukha, H.; Nallappan, K.; Skorobogatiy, M. Toward Real-Time Terahertz Imaging. *Adv. Opt. Photonics* **2018**, *10* (4), 843−938.

(13) Federici, J. F.; Schulkin, B.; Huang, F.; Gary, D.; Barat, R.; Oliveira, F.; Zimdars, D. THz Imaging and Sensing for Security Applications-Explosives, Weapons and Drugs. *Semicond. Sci. Technol.* **2005**, *20* (7), S266−S280.

(14) Siebert, K. J.; Löffler, T.; Quast, H.; Thomson, M.; Bauer, T.; Leonhardt, R.; Czasch, S.; Roskos, H. G. All-Optoelectronic Continuous Wave THz Imaging for Biomedical Applications. *Phys. Med. Biol.* **2002**, *47* (21), 3743−3748.

(15) Cocker, T. L.; Jelic, V.; Gupta, M.; Molesky, S. J.; Burgess, J. A. J.; Reyes, G. D. L.; Titova, L. V.; Tsui, Y. Y.; Freeman, M. R.; Hegmann, F. A. An Ultrafast Terahertz Scanning Tunnelling Microscope. *Nat. Photonics* **2013**, *7* (8), 620−625.

(16) Brenneis, A.; Gaudreau, L.; Seifert, M.; Karl, H.; Brandt, M. S.; Huebl, H.; Garrido, J. A.; Koppens, F. H. L.; Holleitner, A. W. Ultrafast Electronic Readout of Diamond Nitrogen-Vacancy Centres Coupled to Graphene. *Nat. Nanotechnol.* **2015**, *10* (2), 135−139.

(17) Siday, T.; Natrella, M.; Wu, J.; Liu, H.; Mitrofanov, O. Resonant Terahertz Probes for Near-Field Scattering Microscopy. *Opt. Express* **2017**, *25* (22), 27874−27885.

(18) McIver, J. W.; Schulte, B.; Stein, F.-U.; Matsuyama, T.; Jotzu, G.; Meier, G.; Cavalleri, A. Light-Induced Anomalous Hall Effect in Graphene. *Nat. Phys.* **2020**, *16* (1), 38−41.

(19) Prechtel, L.; Song, L.; Schuh, D.; Ajayan, P.; Wegscheider, W.; Holleitner, A. W. Time-Resolved Ultrafast Photocurrents and Terahertz Generation in Freely Suspended Graphene. *Nat. Commun.* **2012**, *3* (1), 1−7.

(20) Jeong, Y.-G.; Bernien, H.; Kyoung, J.-S.; Park, H.-R.; Kim, H.; Choi, J.-W.; Kim, B.-J.; Kim, H.-T.; Ahn, K. J.; Kim, D.-S. Electrical Control of Terahertz Nano Antennas on VO_2 Thin Film. *Opt. Express* **2011**, *19* (22), 21211−21215.

(21) Auston, D. H.; Cheung, K. P.; Smith, P. R. Picosecond Photoconducting Hertzian Dipoles. *Appl. Phys. Lett.* **1984**, *45* (3), 284−286.

(22) Venkatesh, M.; Rao, K. S.; Abhilash, T. S.; Tewari, S. P.; Chaudhary, A. K. Optical Characterization of GaAs Photoconductive Antennas for Efficient Generation and Detection of Terahertz Radiation. *Opt. Mater.* **2014**, *36* (3), 596−601.

(23) Cocker, T. L.; Peller, D.; Yu, P.; Repp, J.; Huber, R. Tracking the Ultrafast Motion of a Single Molecule by Femtosecond Orbital Imaging. *Nature* **2016**, *539* (7628), 263−267.

(24) Jelic, V.; Iwaszczuk, K.; Nguyen, P. H.; Rathje, C.; Hornig, G. J.; Sharum, H. M.; Hoffman, J. R.; Freeman, M. R.; Hegmann, F. A. Ultrafast Terahertz Control of Extreme Tunnel Currents through Single Atoms on a Silicon Surface. *Nat. Phys.* **2017**, *13* (6), 591−598.

(25) Yoshida, S.; Hirori, H.; Tachizaki, T.; Yoshioka, K.; Arashida, Y.; Wang, Z.-H.; Sanari, Y.; Takeuchi, O.; Kanemitsu, Y.; Shigekawa, H. Subcycle Transient Scanning Tunneling Spectroscopy with Visualization of Enhanced Terahertz Near Field. *ACS Photonics* **2019**, *6* (6), 1356−1364.
(26) Muller, M.; Martin Sabanes, N.; Kampfrath, T.; Wolf, M. Phase-Resolved Detection of Ultrabroadband THz Pulses inside a Scanning Tunneling Microscopy Junction. *ACS Photonics* **2020**, *7* (8), 2046−2055.
(27) Lu, Y. F.; Kono, H.; Larkin, T. I.; Rost, A. W.; Takayama, T.; Boris, A. V.; Keimer, B.; Takagi, H. Zero-Gap Semiconductor to Excitonic Insulator Transition in Ta_2NiSe_5. *Nat. Commun.* **2017**, *8* (2), 14408.
(28) Hebling, J.; Yeh, K.-L.; Hoffmann, M. C.; Bartal, B.; Nelson, K. A. Generation of High-Power Terahertz Pulses by Tilted-Pulse-Front Excitation and Their Application Possibilities. *J. Opt. Soc. Am. B* **2008**, *25* (7), B6−B19.
(29) Hoffmann, M. C.; Yeh, K.-L.; Hebling, J.; Nelson, K. A. Efficient Terahertz Generation by Optical Rectification at 1035 nm. *Opt. Express* **2007**, *15* (18), 11706−11713.
(30) Wang, Y.; Chen, Z.; Zhao, Z.; Zhang, L.; Kang, K.; Zhang, Y. Restoration of Terahertz Signals Distorted by Atmospheric Water Vapor Absorption. *J. Appl. Phys.* **2009**, *105* (10), 103105.
(31) Yoshioka, K.; Katayama, I.; Minami, Y.; Kitajima, M.; Yoshida, S.; Shigekawa, H.; Takeda, J. Real-Space Coherent Manipulation of Electrons in a Single Tunnel Junction by Single-Cycle Terahertz Electric Fields. *Nat. Photonics* **2016**, *10* (12), 762−765.
(32) Garg, M.; Kern, K. Attosecond Coherent Manipulation of Electrons in Tunneling Microscopy. *Science* **2020**, *367* (6476), 411−415.
(33) Werdehausen, D.; Takayama, T.; Höppner, M.; Albrecht, G.; Rost, A. W.; Lu, Y.; Manske, D.; Takagi, H.; Kaiser, S. Coherent Order Parameter Oscillations in the Ground State of the Excitonic Insulator Ta_2NiSe_5. *Sci. Adv.* **2018**, *4* (3), 1−7.
(34) Lee, J.; Kang, C.-J.; Eom, M. J.; Kim, J. S.; Min, B.; Il; Yeom, H. W. Strong Interband Interaction in the Excitonic Insulator Phase of Ta_2NiSe_5. *Phys. Rev. B: Condens. Matter Mater. Phys.* **2019**, *99* (7), 075408.
(35) Luo, Y.; Jelic, V.; Chen, G.; Nguyen, P. H.; Liu, Y. R.; Calzada, J. A. M.; Mildenberger, D. J.; Hegmann, F. A. Nanoscale Terahertz STM Imaging of a Metal Surface. *Phys. Rev. B: Condens. Matter Mater. Phys.* **2020**, *102* (20), 205417.

https://dx.doi.org/10.1021/acsphotonics.0c01652
ACS Photonics 2021, 8, 702−708